SUPPLEMENTARY INFORMATION

This supplement is divided into eight sections that explain our approach and calculations in more detail. In section 1 we introduce the conceptual background to our new method of dating the most recent composite Red Sea sea-level record (RSL; Rohling et al., 2009). In section 2 we detail new U/Th datings for the Soreq Cave speleothem $\delta^{18}O$ record. In sections 3 and 4 we describe how we developed an age model for eastern Mediterranean (eMed) core LC21 using Bayesian modelling to further improve our chronostratigraphy. Sections 5 and 6 focus on our new chronology for the RSL record, detailing the LC21-RSL correlation and error propagation. In section 7 we specify the parameters of our probabilistic assessment of the complete RSL dataset. Finally, in section 8 we explain the methods of our lagged correlations and phase analyses between polar climate records and RSL. Online Supplementary Data accompanies this supplement.

1. Conceptual background

We exploit two key properties of the Mediterranean Sea:

1) Eastern Mediterranean (eMed) surface waters are the moisture source for Levantine precipitation, and
2) Mediterranean seawater $\delta^{18}O$ ("$\delta^{18}O_{Med}$") is highly sensitive to sea-level change at the Strait of Gibraltar.

Importantly, these properties (detailed below) relate to well understood, quantifiable physical processes, so our approach has a robust, justifiable basis.
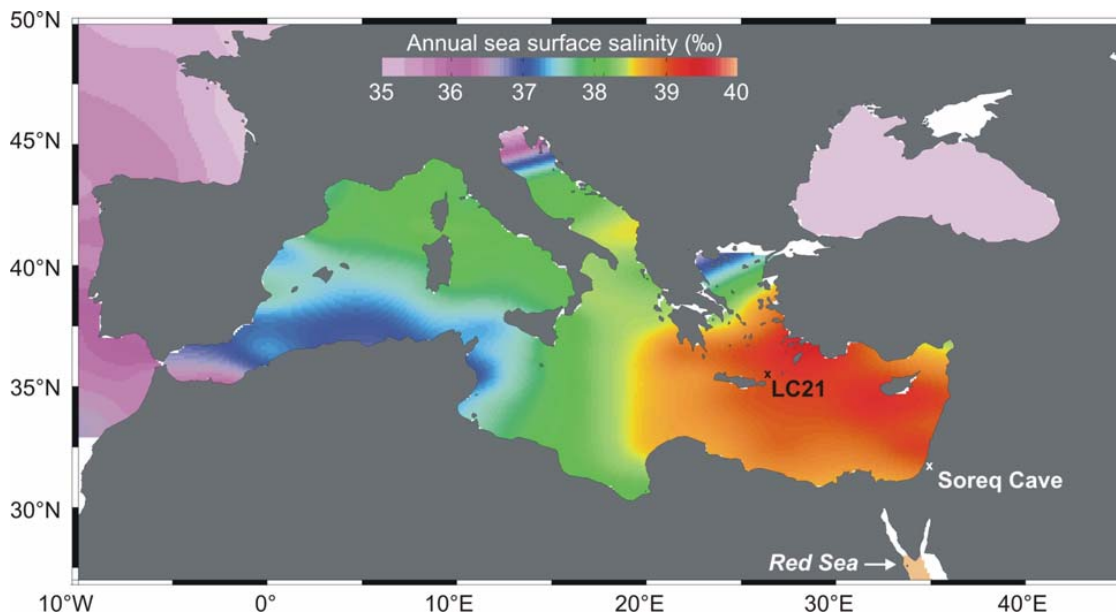

Figure S1 Location map of sites discussed in this study. Annual sea surface salinity is reconstructed from the World Ocean Atlas 2009 dataset using the Ocean Data View (Schlitzer, 2011) software. Areas lacking data are indicated in white.

Studies of terrestrial carbonates (speleothems and snail shells) from the Levant have shown that eMed surface waters are, and have been in the past, the source of moisture precipitating over the Levant (Goodfriend, 1991; Matthews et al., 2000; Bar-Matthews et al., 2000, 2003; McGarry et al., 2004; Almogi-Labin et al., 2009). Therefore, changes in the $\delta^{18}O$ of eMed speleothems are intrinsically linked via a "source water" effect to the $\delta^{18}O$ of eMed surface waters, and hence to

the $\delta^{18}O$ of surface-dwelling planktonic foraminifera. High-resolution speleothem $\delta^{18}O$ records from the Levant (e.g., Bar-Matthews et al., 2003; Gopher et al., 2010; Vaks et al., 2010) have excellent (U-series) age control. Surprisingly, however, there are no continuous, high-resolution records of eMed surface water $\delta^{18}O$ that extend back to the last interglacial (LIG) or further, to complement these speleothem records.

The highly evaporative and semi-enclosed Mediterranean basin is isolated from the open ocean by the narrow and shallow Strait of Gibraltar (284 m) (Fig. S1). These properties cause a "glacial concentration" effect on $\delta^{18}O_{Med}$ similar to that in the Red Sea, albeit to a less extreme extent (Rohling 1994, 1999) (Fig. S2). For example, the glacial-interglacial $\delta^{18}O$ contrast in the open ocean and in the Mediterranean and Red Seas is approximately 1.0, 2.5 and 5.5 ‰, respectively (Schrag et al., 1996; Rohling, 1999; Siddall et al., 2004). As a result, changes in global ice volume/sea-level are reflected in the $\delta^{18}O$ composition of Mediterranean foraminifera in an amplified manner relative to global seawater $\delta^{18}O$, especially in the easternmost sector of the basin where most evaporation occurs (Rohling, 1994, 1999).
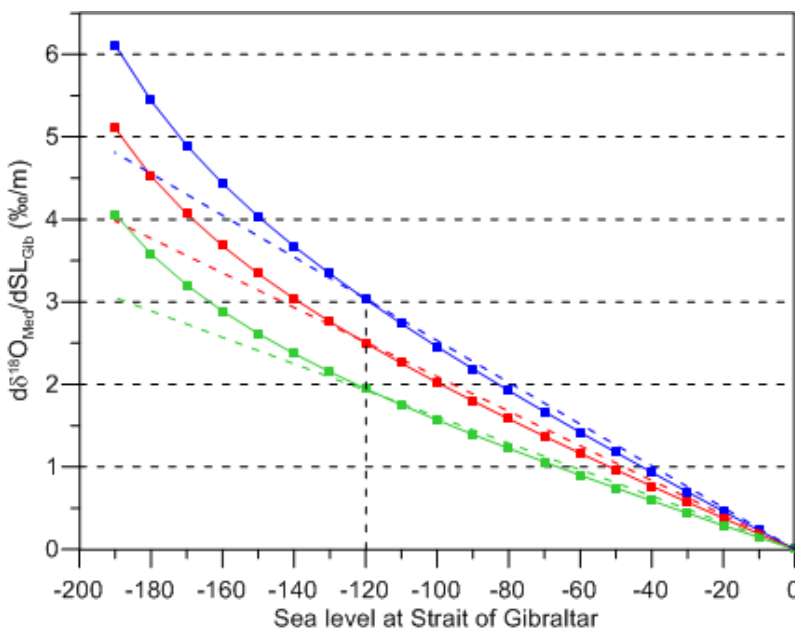

Figure S2 Sea-level sensitivity of Mediterranean $\delta^{18}O$. Changes in Mediterranean seawater $\delta^{18}O$ as a function of varying sea level at the Strait of Gibraltar ($d\delta^{18}O_{Med}/dSL_{Gib}$) are calculated for a relative humidity of 0.65 (blue), 0.70 (red) and 0.75 (green) (see Rohling (1999) for full details of model). For a sea-level change of 120 m (i.e., similar to the glacial-interglacial sea-level change), the relationship is closely approximated by a linear fit (coloured dashed lines) and a $\delta^{18}O_{Med}$ enrichment of 2.5 ± 0.5‰.

We have generated two high-resolution planktonic foraminiferal $\delta^{18}O$ records from a single set of samples from eMed core LC21 using: (1) the surface-dwelling species *Globigerinoides ruber* (white) ("$\delta^{18}O_{ruber}$"), and (2) the deeper-dwelling species *Neogloboquadrina pachyderma* (dextral) ("$\delta^{18}O_{pac}$"), which is commonly found at the base of the euphotic zone near the Deep Chlorophyll Maximum (Pujol and Vergnaud-Grazzini, 1995; Rohling et al., 2004). Core LC21 lies in the 'pool' of highest eMed salinities (Fig. S1) that is the evaporative region of greatest moisture supply to Levantine precipitation. We first, therefore, take advantage of the new $\delta^{18}O_{ruber}$ record, the Soreq Cave $\delta^{18}O$ speleothem record ("$\delta^{18}O_{speleo}$") (Supplementary Data), and the fact that the speleothem source-water derives from eMed surface waters, to transfer the speleothem U-series chronology from Soreq Cave to core LC21.

Next, we exploit the fact that there is a strong sea-level control on both eMed and Red Sea $\delta^{18}O$, to transfer the Soreq-synchronised LC21 chronology to the Red Sea RSL record. This is achieved by correlating RSL with $\delta^{18}O_{pac}$ (Section 4). Because *N. pachyderma* is not associated with surface water masses, any local changes in surface water $\delta^{18}O$ caused by evaporation, precipitation, temperature variations and riverine run-off have minimal effects on its shell $\delta^{18}O$

composition (Rohling et al., 2004), hence the glacial (sea-level) concentration effect will predominantly determine variations in $\delta^{18}O_{pac}$.

Given that the eustatic glacial-interglacial sea-level range is implicitly accounted for in the Red Sea sea-level method, RSL is a good approximation of eustatic sea-level (ESL) variations (Siddall et al., 2003). In this way, we produce the first continuous, high-resolution record of ESL/ice-volume changes over the last full glacial cycle with a detailed radiometric chronology, which is entirely independent of orbital tuning or ice-core timescales.

2. Soreq Cave speleothem U/Th dating

Soreq Cave is located ~60 km inland east of the Mediterranean Sea and 400 m above sea level. Numerous studies of speleothems and rainwater collected from Soreq Cave provide a thorough understanding of past and present speleothem isotopic signatures (e.g., Bar-Matthews et al., 1997, 2000, 2003; Ayalon et al., 1998; Kaufman et al., 1998; Affek et al., 2008). Most of these studies used speleothem datings based on thermal ionisation mass spectrometry (TIMS). The published Soreq Cave $\delta^{18}O$ record has now been updated based on 440 new (previously unpublished) U/Th ages acquired by multi-collector inductively coupled plasma mass spectrometry (MC-ICP-MS) (Supplementary Data). Paired MC-ICP-MS and TIMS datings strongly agree (Fig. S3a), and the new MC-ICP-MS datings substantially increase the dating density of the Soreq Cave age model (Fig. S3b; Supplementary Data). Results from the two approaches are strongly coherent (Fig. S3b), and would therefore produce virtually identical age models for the Soreq Cave $\delta^{18}O$ record, whether used separately or combined.

Speleothems from various locations within Soreq Cave were sampled according to standard procedures (Bar-Matthews et al., 1997). For dating purposes, 0.2-0.5 g of calcite powder was drilled along the speleothem growth axis using 0.8-4.0 mm diameter drill bits. All samples were totally dissolved, with a combination of 7 M HNO_3 and HF, and equilibrated with a mixed $^{229}Th/^{236}U$ spike that was calibrated with gravimetric standards (following Henderson et al., 2001). Both spiked isotopes supplied by Harwell are isotopically clean ($^{229}Th>99.99\%$; $^{236}U=99.97\%$). Samples were loaded onto minicolumns containing 2 ml of Bio-Rad AG 1X8 200-400 mesh resin. U was eluted by 1 M HBr and Th with 6 M HCl. U and Th solutions were evaporated to dryness and the residues dissolved in 2 ml and 5 ml of 0.1 $MHNO_3$, respectively.

U/Th dating was performed using a Nu Instruments Ltd (UK) multi-collector inductively coupled plasma mass spectrometer (MC-ICP-MS) equipped with 12 Faraday cups and 3 ion counters. Each sample was introduced to the MC-ICP-MS through an Aridus® micro-concentric desolvating nebuliser sample introducing system. The instrumental mass bias was corrected (using an exponential equation) by measuring the $^{235}U/^{238}U$ ratio and correcting with the natural $^{235}U/^{238}U$ ratio (137.88). Calibration of ion counters relative to Faraday cups was performed using several cycles of measurement with different collector configurations in each particular analysis. Isotope ratios are given as activity ratios with 2σ uncertainties (Supplementary Data). Uncertainties are propagated from the in-run precision errors (0.4% at 2σ), weighing errors and uncertainties in spike concentrations and isotopic compositions. ^{230}Th and ^{234}U half lives are taken from Cheng et al. (2000). Uncertainties in the half lives of the U-series isotopes are not included in the error propagation.
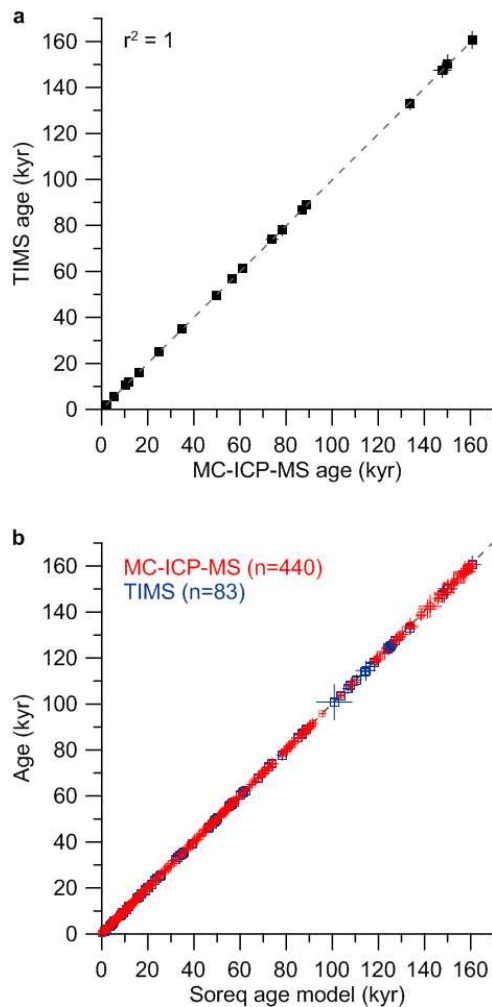
Figure S3 Comparison of MC-ICP-MS and TIMS datings. **a**, Paired MC-ICP-MS and TIMS datings (±2σ) with linear correlation (dashed line, r^2=1). **b**, All MC-ICP-MS (red) and TIMS (blue) datings (±2σ) compared to the Soreq age model (Supplementary Data, sheet 2, column A). All datings follow a linear fit (dashed line).

The U-Th method assumes that all ^{230}Th present in the calcite speleothem is formed *in situ* by radioactive decay of uranium that co-precipitated with the calcite. However, this component is often accompanied by detrital material such as clays, oxides and hydroxides (e.g., Richards and Dorale, 2003; Kaufman et al., 1998). For correction, a ^{232}Th/^{238}U atomic ratio of 1.8±0.25 in the detrital components was used; this value was measured using an isochron method for Soreq Cave speleothems (Kaufman et al., 1998).

3. Age model for core LC21

For the interval 0-40 ka BP, the LC21 age model is constrained by five previously generated radiocarbon datings (Casford et al., 2007), 9 new radiocarbon datings (Table S1), and conclusive identification of two well-dated tephra horizons (the Minoan and the Campanian Ignimbrite, CI, tephra layers) (Fig. S4). New ^{14}C datings (this study) were performed at the University of Oxford Radiocarbon Accelerator Unit on clean, hand-picked planktonic foraminiferal tests with no evidence of pyritization or overgrowth (see Bronk Ramsey et al. (2002) for details of the chemical pretreatment, target preparation and AMS measurement). Calibration of ^{14}C datings into calendar years requires a reservoir age correction, which is a combination of the averaged whole ocean reservoir age (405 yrs) and a local correction ("ΔR"). For Mediterranean marine calcite, ΔR is commonly taken to be 58±85 yrs (Reimer and McCormac, 2002) or 149±30 yrs (Facorellis et al., 1998) depending on whether dated samples were extracted from non-sapropel or sapropel horizons, respectively. A higher ΔR value for

periods of sapropel deposition reflects decreased rates of Mediterranean intermediate- and deep-water ventilation associated with such intervals. Three of our ^{14}C-dated samples were picked from a sapropel, so we use a ΔR value of 149±30 yrs to calibrate these samples and a ΔR value of 58±85 yrs for all other samples (Table S1). All datings (including those of Casford et al. (2007) were calibrated with OxCal (Bronk Ramsey, 2008) using the Marine09 radiocarbon calibration curve. The accuracy of our calibrated ^{14}C datings is further improved by combining sample age and depth information in a Bayesian deposition model (Section 4).
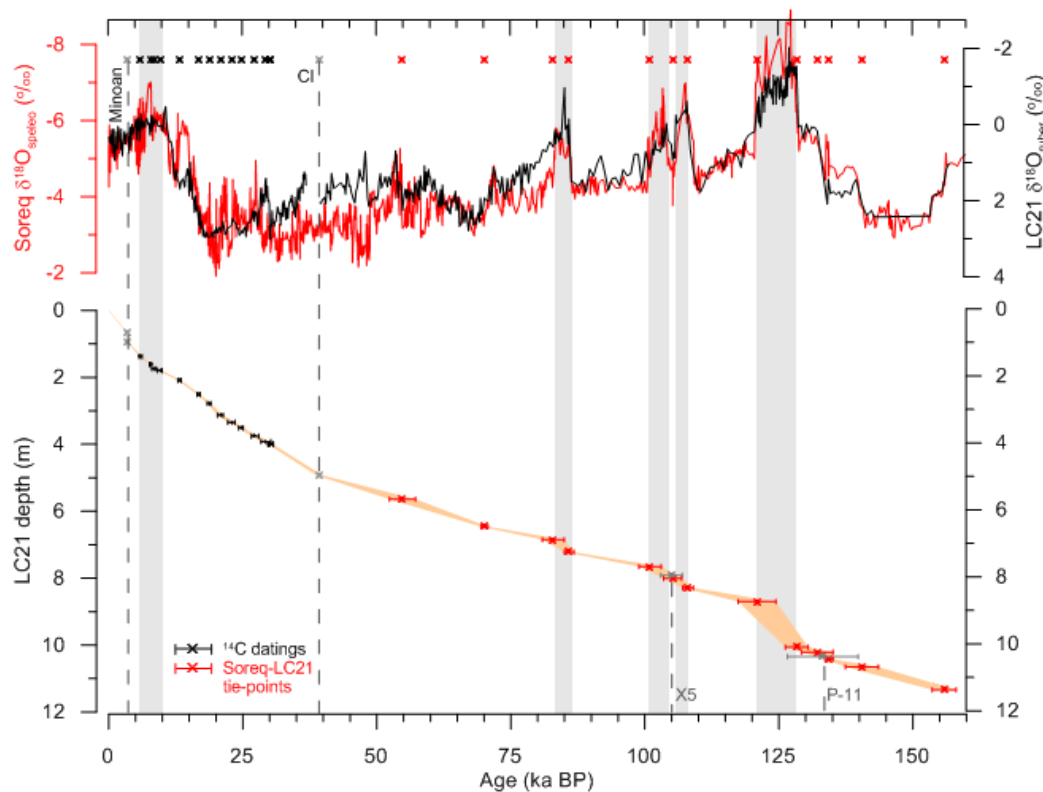

Figure S4 Construction of the LC21 age model. LC21 ^{14}C datings (black crosses) and correlation of the LC21 $\delta^{18}O_{ruber}$ (black) and Soreq Cave $\delta^{18}O_{speleo}$ (red) records, with OxCal-modelled correlation tie-points (red crosses). The Minoan, Campanian Ignimbrite (CI), X5 and P-11 tephra horizons (grey crosses and dashed lines) and intervals of sapropel deposition (grey rectangles) are also indicated. Superimposed on the LC21 age-depth model (orange fill) are the error margins of the ^{14}C datings, Soreq-LC21 tie-points and tephra horizons (black, red and grey error bars (2σ), respectively).

For the interval 40-150 ka BP, we used Analyseries (Paillard, 1996) to graphically correlate the $\delta^{18}O_{ruber}$ and $\delta^{18}O_{speleo}$ records (Fig. S4). As mentioned above, there is a direct physical process linking the $\delta^{18}O$ of calcite precipitated in eMed surface waters and in Levantine caves. It follows that there will be a signal common to both $\delta^{18}O_{ruber}$ and $\delta^{18}O_{speleo}$ on which any local $\delta^{18}O$ variations are superimposed. On long (orbital) timescales, eMed surface waters are periodically affected by intense freshening, and thus $\delta^{18}O$ depletion, caused by flooding of the Nile and North African wadi systems as a result of intensification and northward penetration of the African monsoon during precession minima (Rohling et al., 2002, 2004; Larrasoaña et al., 2003). These $\delta^{18}O$ depletions, together with sea level-controlled variations in $\delta^{18}O_{Med}$, are clearly evidenced by the good general agreement between $\delta^{18}O_{ruber}$ and $\delta^{18}O_{speleo}$. We therefore only correlate these major transitions in $\delta^{18}O_{ruber}$ and $\delta^{18}O_{speleo}$. In this way we transfer the U-series speleothem chronology to core LC21.

Our Soreq-LC21 correlation is validated by identification of two further tephra horizons at 7.915 m and 10.345 m in core LC21. These correlate with the X5 and P-11 tephras that have been dated at 105 ±2 ka BP (Kraml, 1997) and, indirectly, at 132.3 ±5.7 to 133.5 ±6.2 ka BP (Mahood and Hildreth, 1986), respectively (Fig. S4). Next, we applied a Bayesian deposition model using the OxCal programme (Bronk Ramsey, 2008), to derive a best-case chronology for LC21 with well-defined uncertainties.

4. OxCal Bayesian models

The chronostratigraphy of a sediment core is, in effect, a series of probability functions, and information of a probabilistic nature can be mathematically combined using the Bayes Theorem. OxCal achieves this using the Markov Chain Monte Carlo (MCMC) sampling method (Gilks et al., 1996) and Bayesian algorithms to create "*posterior*" probability densities for each point in a sedimentary sequence. Specifically, OxCal builds a "*prior*" model from information about the deposition of the sequence and the actual dates. Here we use the "Sequence" and "Poisson" OxCal models. The simple Sequence model allows wide variations in sedimentation rate and makes minimal *a priori* assumptions, assuming only that there are no age reversals in the sedimentary sequence. The Sequence model is also applicable when coherent depth information is lacking, as is the case for the Soreq Cave composite speleothem record. The Poisson model includes depth information and is therefore more appropriate for the LC21 datings. Previous studies have demonstrated that the Sequence and Poisson models can significantly improve the precision of an age model whilst retaining accuracy (Bronk Ramsey 2000; Blockley et al., 2007).

Our prior models consist of dates and uncertainties in the form of a normal (Gaussian) probability distribution (the "*likelihood*"), with an uncertainty σ about the mean μ. The dating information is from Soreq Cave (Supplementary Data), LC21 (Table S1) and from the Minoan (Manning et al., 2006) and CI (De Vivo et al., 2001) tephra horizons). The Soreq-LC21 tie-points were inserted into the OxCal Sequence model as a blank age and uncertainty at the relevant chronostratigraphic level obtained from the correlation, in order to determine a posterior probability density distribution for each tie-point.

OxCal assesses the statistical robustness of a model run by calculating an "Agreement Index" (AI), which is determined by the area of overlap between the probability density distributions of the *prior* (unmodelled) data and the posteriors. The higher the AI, the better the agreement, and the acceptance threshold for a posterior density is an AI >60% (Bronk Ramsey, 2008). In both of our models, overall agreement between the priors and the posteriors is high (AI >99% for most [97%] of the dates in the Sequence model; AI >87% for all dates in the Poisson model), which implies that our modelled ages and uncertainties are statistically robust. The final Soreq Cave chronology is accurate to within ±500 years for most of the dates (72%), and has a maximum uncertainty of ±2686 years. Only 3% of the dates have an uncertainty >1500 years.

The modelled ^{14}C dates and tephra ages were then used to establish the LC21 chronology (by linear interpolation) for the interval 0-40 ka BP. After rescaling the $\delta^{18}O_{speleo}$ record using the modelled U/Th dates, the $\delta^{18}O_{rub}$ and $\delta^{18}O_{speleo}$ records were re-synchronised for the interval 40-150 ka BP (see main-text Fig. 1a). Finally, the completed LC21 age model was used to date the $\delta^{18}O_{pac}$ record, and we were then ready to tune RSL to $\delta^{18}O_{pac}$ (see below).

5. New chronology for RSL

Our new chronology for the Red Sea sea-level record (RSL) is a product of two synchronisations: most of the record (22-150 ka BP) was tuned to the LC21 $\delta^{18}O_{pac}$ record,

whereas the last deglacial interval (0-22 ka BP) was correlated with the global sea-level probability curve of Stanford et al. (2011) (see main text and main-text Fig. 1b). We emphasise again that correlation of the RSL and $\delta^{18}O_{pac}$ records is justified on the basis of a sound, quantitative understanding of the common process (sea-level change) that causes first-order similarity between the records (Fig. S2 and main-text Fig. S1b).

To tune RSL to $\delta^{18}O_{pac}$ we limit our ties to clearly identifiable transitions common to both records, and minimise the number of ties (n=15) required for a good synchronisation (main-text Fig. 1). It is common practice, when graphically correlating records, to anchor them at the mid-point of corresponding transitions, rather than using peaks or troughs in the records. We follow this approach, but make one exception for the tie-point at the base of termination II (main-text Fig. 1). We chose this position (at 136 ka) because an unambiguous tie-point is lacking over the transition due to the different step-wise structures of the two records; the records are much more similar at the base of the transition which means that we can more confidently assign a tie-point here. We also avoid placing tie-points within the time intervals of sapropel deposition in core LC21. It is well known that periods of sapropel formation were associated with significant hydrological changes in the eMed, hence it is likely that $\delta^{18}O_{pac}$ does not solely reflect changes in sea level at these times (Rohling et al., 2004).

Tuning RSL over the last deglacial interval (0-22 ka BP) was straightforward owing to the smooth structure of the (target) probabilistic sea-level curve (main-text Fig. 1). The most contentious issue was where to anchor the base of this section of the RSL record, which lacks structure from 14 to 22 ka BP due to an aplanktonic zone in Red Sea sediments. The consequently increased uncertainty associated with the tie-points at 12.45, 15.55 and 17.45 ka BP is considered in our full propagation of age errors (section 6 below).

Next, we converted RSL (on its new chronology) into $\delta^{18}O_{Med}$-equivalent values using a scaling of 2.5±0.5 ‰ per 120 m sea-level change (main-text Fig. 1). This exercise demonstrates that for most of the last glacial cycle, $\delta^{18}O_{pac}$ varies within the uncertainties of a theoretical $\delta^{18}O_{Med}$-equivalent RSL curve, thus providing further evidence that lower frequency variations in $\delta^{18}O_{pac}$ correspond to the timing of sea-level change at the Strait of Gibraltar. In MIS 5a, 5c and 5e there are distinct intervals of $\delta^{18}O_{pac}$ 'overshoots', which largely coincide with deposition of sapropels S3, S4 and S5. This is to be expected and does not invalidate our tuning or approach because no tie-points were placed within these intervals (see above).

6. Propagation of RSL age uncertainties

We now rigorously determine the chronological uncertainties in our new RSL record. This involves propagating all uncertainties (a-k) from the three correlations (i-iii) as summarised below.
  i) From the Soreq-LC21 correlation:
      a) radiometric dating error of Soreq Cave speleothems, LC21 planktonic foraminifera, and the Minoan and CI tephras,
      b) sample spacing in the Soreq $\delta^{18}O_{speleo}$ record,
      c) sample spacing in the LC21 $\delta^{18}O_{ruber}$ record, and
      d) extra uncertainty allowance for more ambiguous (category 2 and 3) tie-points.
  ii) From the LC21-RSL correlation:
      e) total error carried over from the Soreq-LC21 correlation (i above),
      f) sample spacing in the RSL record (for the interval 22-150 ka BP),
      g) sample spacing in the $\delta^{18}O_{pac}$ record, and
      h) extra uncertainty allowance for category 2 and 3 tie-points.
  iii) From the deglacial-RSL correlation:

j) methodological uncertainty in the Stanford et al. (2011) probabilistic sea-level curve, and

k) sample spacing in the RSL record (for the interval 0-22 ka BP).

These uncertainties are determined as follows: (a) is derived from our OxCal Sequence model; (b), (c), (f), (g) and (k) relate to the age difference between tie-points and nearest neighbouring samples in the $\delta^{18}O_{speleo}$, $\delta^{18}O_{ruber,}$ RSL and $\delta^{18}O_{pac}$ records, respectively. For (c), depth differences in core LC21 were converted into an equivalent age uncertainty; (e) is deduced by interpolation after combining uncertainties a-d (see below); (j) is taken from Stanford et al. (2011); (d) and (h) are imposed uncertainties and may be ±0.5 or ±1 kyr for category 2 and 3 tie-points, respectively (see main text, main-text Fig. 1, and Table S2).

We combined these uncertainties in a mean squared estimate (MSE) at the 95% probability level for the Soreq-LC21 correlation ("MSE_i"), the LC21-RSL correlation ("MSE_{ii}"), and the deglacial-RSL correlation ("MSE_{iii}"), as defined by:

$$MSE_i = \sqrt{\{a^2 + b^2 + (c+d)^2\}},$$
$$MSE_{ii} = \sqrt{\{e^2 + (f+g+h)^2\}}, \text{ and}$$
$$MSE_{iii} = \sqrt{\{j^2 + k^2\}}.$$

First, we calculated the total uncertainty for every Soreq-LC21 tie-point (MSE_i; red crosses and bars in Fig. S5). Next, we interpolated between successive lower and upper error margins of the Soreq-LC21 tie-points in order to produce a continuous error margin for the entire LC21 age-depth model (orange envelope in Fig. S5). We then determined the position of the LC21-RSL tie-points within the LC21 age-depth model, as well as their uncertainties (e) associated with the Soreq-LC21 correlation (green crosses and bars in Fig. S5). This involved converting the age of every LC21-RSL tie-point into an equivalent LC21 depth, and then linearly interpolating between each LC21-RSL tie-point and the error margins of its neighbouring Soreq-LC21 tie-points. We could now calculate MSE_{ii} (Table S2).
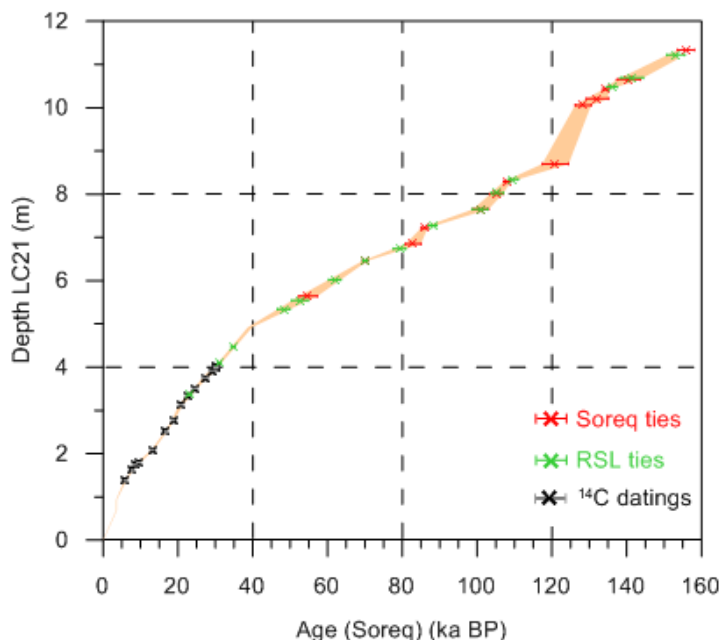
Figure S5 Interpolation of uncertainties for RSL. LC21 age-depth model (orange fill) with tie-points and 2σ uncertainties for the Soreq-LC21 (red crosses and bars) and LC21-RSL (green crosses and bars) correlations. LC21 ^{14}C datings are also shown (black crosses and 2σ error bars).

Determining MSE_{iii} required no imposed uncertainties for sample spacing because our RSL record and the Stanford et al. (2011) probabilistic sea-level curve both follow the same broad

trend, without any ambiguous peaks/troughs with respect to potential correlation points (Table S2). Finally, linear interpolation between the total LC21-RSL and deglacial-RSL tie-point uncertainties (MSE_{ii} and MSE_{iii}) produced a chronological uncertainty for every datapoint in the full RSL record. The latter is needed before we can produce a probabilistic analysis of the sea-level curve for the last full glacial cycle (see below).

7. Probabilistic analysis of Red Sea sea-level record

In order to determine confidence limits to RSL that fully account for the combined uncertainties in both age and sea-level reconstruction (main-text Fig. 2), we have defined normal distributions around each datapoint, based on the mean datapoint values and their standard deviations in both the age and sea-level directions (where the standard deviation for each point in the sea-level reconstruction method is ±6 m; Siddall et al., 2003, 2004). These probability intervals account for all of the combined uncertainties in both age and sea-level values and represent "worst case" propagation scenarios, given that no correlation was considered between any of the uncertainties. We then made N=1000 new records using independent random perturbations of all points within their probability distributions. This gives a 'sample' of 1000 RSL 'realisations' per equally spaced time step of 125 years (close to the average time resolution of the original data). For each 'sample', we determine the 95% confidence limit (from percentile counts) and the RSL value of the probability maximum ("RSL_{P-max}"); the latter provides the 'best fit' RSL curve from the Red Sea data. The record of RSL_{P-max} from the 1000 realisations per time step has been smoothed with a moving 500-year Gaussian filter to remove spurious jumps, and is determined with a precision of ±7 m (95%).

The 95% confidence limits from the 1000 RSL realisations provide insight into the tolerance to scatter of any new sea-level data (with their own uncertainties) relative to the Red Sea sea-level record presented here. If new data consistently fall outside the limits, they may need to be subjected to a detailed outlier analysis, whereas if they fall inside the limits, they may be considered coherent with the Red Sea sea-level information.

For each individual RSL realisation, we also calculated the rates of change. This was achieved after smoothing each realisation with a 500-year moving Gaussian filter in order to remove sample-to-sample noise that would produce spurious rate jumps. We determined, per time step, the 95% confidence limit and the probability maximum of the rates of change ("$dRSL_{P-max}/dt$"). Based on 1000 realisations, we find that $dRSL_{P-max}/dt$ has a precision of ±8 m/kyr, at the 95% confidence level (main-text Fig. 3c).

8. Lagged correlations and phase analyses of ice-core records and RSL

We further investigate the relationship between changes in polar climate and global ice volume. We use $\delta^{18}O$ records from the European Project for Ice Coring in Antarctica (EPICA) Dronning Maud Land (EDML) (EPICA, 2006) and from the North Greenland Ice-core Project (NGRIP) (North Greenland Ice Core Project Members, 2004) as approximations of polar climate variations because they are the best-dated and most highly resolved ice-core climate records for the last glacial cycle. The RSL record closely approximates eustatic sea level (Siddall et al., 2003), and hence global ice-volume change.

First we regressed the ice-core records against RSL for intervals of both sea-level rise and fall. Our aim here is to establish whether the polar climate: ice-volume relationship varies between these intervals. We smoothed the RSL record with a 1 kyr moving Gaussian filter at 100 year age-steps ("RSLs") in order to remove sample-to-sample "noise" and reveal meaningful trends, and interpolated the EDML and NGRIP $\delta^{18}O$ records to the same 100 year age-steps. This

exercise demonstrates that the polar climate: sea-level relationship shows no significant hysteresis (Fig. S6), and means that we can investigate phase offsets throughout the entire records using lagged correlation and cross-spectral analyses (see below).
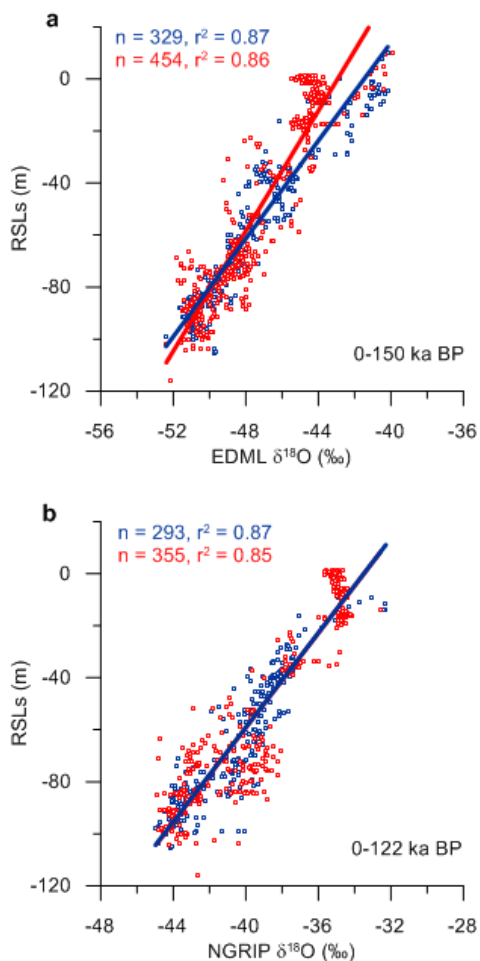

a

n = 329, r² = 0.87
n = 454, r² = 0.86

0-150 ka BP

Figure S6 Regression plots of Antarctic and Greenland temperature versus the smoothed Red Sea sea-level record (RSLs). Optimum linear correlations and their coefficients (r^2) are given for datapoints (n) corresponding to intervals of rising (red) and falling (blue) sea level. **a**, EDML $\delta^{18}O$ against RSLs for the interval 0-150 ka BP. **b**, NGRIP $\delta^{18}O$ against RSLs for the interval 0-122 ka BP.

We applied the same Gaussian smoothing to the ice-core records (EDMLs, NGRIPs) in order to calculate their first derivatives (dEDMLs/dt, dNGRIPs/dt), and then performed a series of lagged correlations (0 to ±2000 years) at 100 yr intervals on: 1) EDMLs vs. RSL_{pmax}, 2) NGRIPs vs. RSL_{pmax}, 3) dEDMLs/dt vs. $dRSL_{pmax}$/dt, and 4) dNGRIPs/dt vs. $dRSL_{pmax}$/dt (main-text Fig. 3a,b). This straightforward exercise allows us to see which phase offsets produce the best correlation between polar climate and ice volume, and between their rates of change; the absolute values of the correlation coefficients are therefore of secondary importance here.

We find optimum correlations when changes in ice volume (sea-level) lag changes in Antarctic and Greenland climate by 100-400 and 200-400 years, respectively (main-text Fig. 3a,b), which suggests that changes in ice volume are equally in phase with changes in both Antarctic and Greenland climate. The strongest correlation between rates of change in RSL and in Antarctic and Greenland climate is achieved with a 100-year and zero lag, respectively (main-text Fig. 3a,b). Taken together, these striking results suggest that a comparatively short (centennial-scale) response time characterises the polar climate-ice volume relationship. This finding requires further scrutiny, given its potentially far-reaching consequences in the context of current global warming trends. For that purpose, we take a more quantitative approach by performing Blackman-Tukey cross-spectral analyses (using the Analyseries software; Paillard, 1996) on the full EDML $\delta^{18}O$, NGRIP $\delta^{18}O$, and RSL records, as well as on RSLs and RSL_{pmax}, for the time

intervals 0-150 and 30-80 ka BP (Table S3). First we removed all frequencies less than 0.03 (this includes all obliquity and eccentricity-related frequencies) using a notch filter with bandwidth of 0.03 (= 33 kyr periodicity); the time series are not sufficiently long for meaningful spectral analyses of these orbital cycles. We therefore focus on sub-orbital and, to a lesser extent, precessional frequencies (our studied time interval contains six precession cycles, which is an inadequate number for a robust phase analysis).

We observe high coherence between changes in polar climate and ice volume at precessional and sub-precessional periodicities, with zero to multi-centennial response times (Table S4). Consistent results for the different RSL records and time intervals validate the precision of these analyses. Changes in Greenland climate and ice volume are tightly coupled at the 4.5 and ~9.6 kyr periodicities (zero lag) and are closely coupled at the 6.4 and precession periodicities (100-300 years ice-volume lead). At sub-precessional periodicities, rates of change in Greenland climate and in ice volume are also closely coupled (100-300 year ice-volume lead).

We observe larger phase offsets between ice-volume variability and Antarctic climate changes (rather than those of Greenland). Changes in ice volume lead Antarctic climate variability at the precession periodicity (by 400 years) and lag it at the half-precession and 6.8 kyr periodicities (by 600-700 years). A similar sign and magnitude of phase offset is observed between rates of change in ice volume and in Antarctic climate at the precession and half-precession periodicities.

The results of the phase analyses for the NGRIP record clearly uphold the results of our lagged correlations (main-text Fig. 3), and imply that ice-volume and Greenland temperature variability are tightly coupled. With respect to the phase relationship between Antarctic climate and ice volume variability, lagged correlations suggest a closer coupling than that indicated by cross-spectral phase analyses. However, given that there is a less distinct 'optimum' in the EPICA-RSL lagged correlations, and that uncertainty margins of the phase offsets may reach ±400 years, we conclude that the results of the two approaches are not incompatible and are dependent on the different frequencies of variability in the records.

Our regression and cross-spectral analyses demonstrate that changes in polar climate and ice volume are coupled, and that response times may be relatively rapid (centennial-scale). This type of phase analysis is possible for the first time because our new chronology has excellent centennial-multi-centennial age control, and because it is entirely independent of orbital tuning and ice-core age models.

References

Affek, H.P., Bar-Matthews, M., Ayalon, A., Matthews, A., Eiler, J.M. 2008. Glacial/interglacial temperature variations in Soreq Cave speleothems as recorded by 'clumped isotope' thermometry. Geochimica et Cosmochimica Acta 72, 5351-5360.

Almogi-Labin, A., Bar-Matthews, M., Shriki, D., Kolosovsky, E., Paterne, M., Schilman, B., Ayalon, A., Aizenshtat, Z., Matthews, A. 2009. Climatic variability during the last ~90 ka of the southern and northern Levantine Basin as evident from marine records and speleothems. Quaternary Science Reviews 28, 2882-2896.

Ayalon, A., Bar-Matthews, M., Sass, E. 1998. Rainfall-recharge relationships within a karstic terrain in the Eastern Mediterranean semi-arid region, Israel: $\delta^{18}O$ and δD characteristics. Journal of Hydrology 207, 18-31.

Bar-Matthews, M., Ayalon, A., Kaufman, 1997. A. Late Quaternary paleoclimate in the Eastern Mediterranean region from stable isotope analysis of speleothems at Soreq Cave, Israel. Quaternary Research 47, 155-168.

Bar-Matthews, M., M., Ayalon, A., Kaufman, A. 2000. Timing and hydrological conditions of sapropel events in the Eastern Mediterranean, as evident from speleothems, Soreq cave, Israel. Chemical Geology 169, 145-156.

Bar-Matthews, M., Ayalon, A., Gilmour, M., Matthews, A., Hawkesworth, C.J. 2003. Sea–land oxygen isotopic relationships from planktonic foraminifera and speleothems in the Eastern Mediterranean region and their implication for paleorainfall during interglacial intervals. Geochimica et Cosmochimica Acta 67, 3181-3199.

Bronk Ramsey, C. 2000. Comment on the use of Bayesian statistics for ^{14}C dates of chronologically ordered samples: a critical analysis. Radiocarbon 42, 199-202.

Bronk Ramsey, C., Higham, T.F.G., Owen, D.C., Pike, A.W.G., Hedges, R.E.M. 2002. Radiocarbon dates from the Oxford AMS system: Archaeometry Datelist 31. Archaeometry 44, Supplement 1, 1-150.

Bronk Ramsey, C. 2008. Deposition models for chronological records. Quaternary Science Reviews 27, 42-60.

Blockley, S.P.E., Blaauw, M., Bronk Ramsey, C., van der Plicht, J. 2007. Building and testing age models for radiocarbon dates in Lateglacial and Early Holocene sediments. Quaternary Science Reviews 26, 1915-1926.

Casford, J.S.L., Abu-Zied, R., Rohling, E.J., Cooke, S., Fontanier, Ch., Leng, M., Millard, A., Thomson, J. 2007. A stratigraphically controlled multi-proxy chronostratigraphy for the eastern Mediterranean. Paleoceanography 22, PA4215, doi:10.1029/2007PA001422.

Cheng, H., Edwards, R.L., Hoff, J., Gallup, C.D., Richards, D.A., Asmerom, Y. 2000. The half-lives of uranium-234 and thorium-230. Chemical Geology 169, 17-33.

Cleveland, W.S., Devlin, S.J. 1988. Locally-weighted regression: an approach to regression analysis by local fitting. Journal of the American Statistical Association 83, 596-610.

De Vivo, B., Rolandi, G., Gans, P.B., Calvert, A., Bohrson, W.A., Spera, F.J., Belkin, H.E. 2001. New constraints on the pyroclastic eruptive history of the Campanian volcanic plain (Italy). Mineralogy and Petrology 73, 47-65.

EPICA Community Members 2006. One-to-one coupling of glacial climate variability in Greenland and Antarctica. Nature 444, 195-198.

Facorellis, Y., Maniatis, Y., Kromer, B. 1998. Apparent ^{14}C ages of marine mollusk shells from a Greek island: calculation of the marine reservoir effect in the Aegean Sea. Radiocarbon 40, 963-973.

Gilks, W., Richardson, S., Spiegelhalter, D. (Eds.) 1996. Markov Chain Monte Carlo in Practice. Chapman & Hall, London.

Goodfriend, G.A. 1991. Holocene trends in ^{18}O in land snail shells from the Negev Desert and their implications for changes in rainfall source areas. Quaternary Research 35, 417-426.

Gopher, A., Ayalon, A., Bar-Matthews, M., Barkai, R., Frumkin, A., Karkanas, P., Shahack-Gross, R. 2010. The chronology of the late Lower Paleolithic in the Levant based on U-Th ages of speleothems from Qesem Cave, Israel. Quaternary Geochronology 5, 644-656.

Henderson, G.M., Slowey, N.C., Fleisher, M.Q. 2001. U-Th dating of carbonate platform and slope sediments. Geochimica et Cosmochimica Acta 65, 2757-2770.

Kaufman, A., Wasserburg, G.J., Porcelli, D., Bar-Matthews, M., Ayalon, A., Halicz, L. 1998. U-Th isotope systematics from the Soreq cave, Israel and climatic correlations. Earth and Planetary Science Letters 156, 141-155.

Kraml, M. 1997. Laser-^{40}Ar/^{39}Ar Datierungen an distalen marinen Tephren des jung-quartären mediterranen Vulkanismus (Ionisches Meer, METEOR-Fahrt 25/4). Doctoral Thesis, Universität Freiburg im Breisgau, 216pp.

Larrasoaña, J.C., Roberts, A.P., Rohling, E.J., Winklhofer, M., Wehausen, R. 2003. Three million years of monsoon variability over the northern Sahara. Climate Dynamics 21, 689-698.

Mahood, G.A., Hildreth, W. 1986. Geology of the peralkaline volcano at Pantelleria, Strait of Sicily. Bulletin of Volcanology 48, 143-172.

Manning, S.W., Bronk Ramsey, C., Kutschera, W., Higham, T., Kromer, B., Steier, P., Wild, E.M. 2006. Chronology for the Aegean Late Bronze Age 1700-1400 BC. Science 312, 565-569.

Matthews, A., Ayalon, A., Bar-Matthews, M. 2000. D/H ratios of fluid inclusions of Soreq Cave (Israel) speleothems as a guide to the eastern Mediterranean meteoric line relationships in the last 120 ky. Chemical Geology 166, 183-191.

McGarry, S., Bar-Matthews, M., Matthews, A., Vaks, A., Schilman, B., Ayalon, A. 2004. Constraints on hydrological and paleotemperature variations in the eastern Mediterranean region in the last 140 ka given by the δD values of speleothem fluid inclusions. Quaternary Science Reviews 23, 919-934.

North Greenland Ice Core Project Members 2004. High-resolution record of Northern Hemisphere climate extending into the last interglacial period. Nature 431, 147-151.

Paillard, D. 1996. Macintosh Program performs time-series analysis. Eos Transactions, American Geophysical Union 77, 39.

Pujol, C., Vergnaud-Grazzini, C. 1995. Distribution patterns of live planktic foraminifers as related to regional hydrography and productive systems of the Mediterranean Sea. Marine Micropaleontology 25, 187-217.

Reimer, P.J., McCormac, F.G. 2002. Marine radiocarbon reservoir corrections for the Mediterranean and Aegean Seas. Radiocarbon 44, 159-166.

Richards, D.A., Dorale, J.A. 2003. Uranium-series chronology and environmental applications of speleothems. Reviews in Mineralogy and Geochemistry 52, 407-460.

Rohling, E.J. 1994. Review and new aspects concerning the formation of Mediterranean sapropels. Marine Geology 122, 1-28.

Rohling, E.J. 1999. Environmental control on Mediterranean salinity and δ^{18}O. Paleoceanography 14, 706-715.

Rohling, E.J., Cane, T.R., Cooke, S., Sprovieri, M., Bouloubassi, I., Emeis, K.C., Schiebel, R., Kroon, D., Jorissen, F.J., Lorre, A., Kemp, A.E.S. 2002. African monsoon variability during the previous interglacial maximum. Earth and Planetary Science Letters 202, 61-75.

Rohling, E.J., Sprovieri, M., Cane, T.R., Casford, J.S.L., Cooke, S., Bouloubassi, I., Emeis, K.C., Schiebel, R., Hayes, A., Jorissen, F.J., Kroon, D. 2004. Reconstructing past planktic foraminiferal habitats using stable isotope data: a case history for Mediterranean sapropel S5. Marine Micropaleontology 50, 89-123.

Rohling, E.J., Grant, K., Bolshaw, M., Roberts, A.P., Siddall, M., Hemleben, C., Kucera, M. 2009. Antarctic temperature and global sea level closely coupled over the past five glacial cycles. Nature Geoscience 2, 500-504.

Schlitzer, R. 2011. Ocean Data View. http://odv.awi.de.

Schrag, D.P., Hampt, G., Murray, D.W. 1996. Pore fluid constraints on the temperature and oxygen isotopic composition of the glacial ocean. Science 272, 1930-1932.

Siddall, M., Smeed, D.A., Hemleben, C., Rohling, E.J., Schmelzer, I., Peltier, W.R. 2004. Understanding the Red Sea response to sea level. Earth and Planetary Science Letters 225, 421-434.

Stanford, J.D., Hemingway, R., Rohling, E.J., Challenor, P.G., Medina-Elizalde, M., Lester, A.J. 2011. Sea-level probability for the last deglaciation: a statistical analysis of far-field records. Global and Planetary Change 79, 193-203.

Vaks, A., Bar-Matthews, M., Matthews, A., Ayalon, A., Frumkin, A. 2010. Middle-Late Quaternary paleoclimate of northern margins of the Saharan-Arabian Desert: reconstruction from speleothems of Negev Desert, Israel. Quaternary Science Reviews 29, 2647-2662.

Table S1 Core LC21 radiocarbon dating results.

Depth in core (m)	Uncalibrated AMS ^{14}C age $\pm 2\sigma$ (ka BP)	Calibrated ^{14}C age $\pm 2\sigma$ (ka BP)	AI (%)	Reference
1.38	5.590 ± 0.120	5.936 ± 0.244	99.8	Casford et al. (2007)
1.62	7.480 ± 0.120	7.801 ± 0.146*	99.3	Casford et al. (2007)
1.74	8.120 ± 0.120	8.437 ± 0.140*	99.9	Casford et al. (2007)
1.80	9.010 ± 0.140	9.533 ± 0.174*	100.7	Casford et al. (2007)
2.09	11.770 ± 0.160	13.199 ± 0.236	102.5	Casford et al. (2007)
2.51	14.070 ± 0.100	16.769 ± 0.248	103.5	This study
2.78	15.970 ± 0.110	18.719 ± 0.182	99.9	This study
3.13	17.925 ± 0.140	20.821 ± 0.498	99.5	This study
3.34	19.625 ± 0.150	22.876 ± 0.512	99.7	This study
3.51	21.110 ± 0.180	24.655 ± 0.372	98.8	This study
3.76	23.010 ± 0.300	27.291 ± 0.660	99.6	This study
3.92	24.830 ± 0.920	29.315 ± 0.866	87.2	This study
3.99	25.730 ± 0.260	30.146 ± 0.480	101.6	This study
4.01	25.980 ± 0.280	30.242 ± 0.462	91.7	This study

AI = Agreement Index (see Section 3). Material extracted from sapropel S1 (*) has been calibrated using a ΔR value of 149 ± 30 years (Facorellis et al., 1998; see Section 3).

Table S2 Summary of RSL tie-point uncertainties (see Part 6 for definitions of uncertainties e, f, g, h, j and k).

a) RSL-$\delta^{18}O_{pac}$ correlation. Tie-points are classed as category 1 (black), 2 (blue) and 3 (red)

RSL tie-point	Uncertainty (e) (ka)	Uncertainty (f) (ka)	Uncertainty (g) (ka)	MSE_{ii} (ka)
1	0.6263	2.970	0.405	**5.84**
2	0.4786	0.214	0.197	**0.56**
3	0.5270	0.207	0.196	**0.60**
4	1.6636	0.310	0.868	**1.90**
5	2.1804	0.266	0.434	**2.24**
6	1.6103	0.270	0.373	**2.10**
7	0.6659	0.989	0.659	**1.36**
8	1.6511	0.682	0.659	**1.90**
9	1.0691	0.722	1.390	**1.90**
10	2.0634	0.374	1.026	**2.71**
11	1.6395	0.939	0.842	**2.07**
12	1.3088	0.434	1.260	**1.87**
13	1.3759	0.257	1.067	**2.16**
14	3.0228	0.194	0.896	**3.38**
15	2.3858	0.796	0.448	**3.79**

b) RSL-deglacial correlation

RSL tie-point	Uncertainty (j) (ka)	Uncertainty (k) (ka)	MSE_{iii} (ka)
1	0	0.069	**0.069**
2	0.20	0.129	**0.238**
3	0.20	0.206	**0.287**
4	0.10	0.584	**0.592**
5	0.20	1.504	**1.517**
6	0.35	3.593	**3.610**
7	0.75	3.593	**3.670**

Table S3 Summary of phase analyses of ice-core and RSL records. Lags (and 2σ uncertainties) ≥0.6 kyr are highlighted (red).

	Periodicity (kyr)	Coherency (%)	Lag (kyr)	Lag uncertainty (kyr)
EDML vs. RSL	25	91	-0.4	±0.4
	11.6	85	0.7	±0.3
	6.8	66	0.6	±0.3
dEDML/dt vs. dRSL/dt	26.3	92	-0.5	±0.4
	11.9	86	0.7	+0.3/-0.2
NGRIP vs. RSL	20.8	89	-0.2	±0.4
	9.6	68	0.1	-0.5/+0.4
	6.4	81	-0.3	-0.1/+0.2
	4.5	80	0.0	-0.1/+0.2
dNGRIP/dt vs. dRSL/dt	27.8	89	0.5	±0.5
	10	76	-0.3	±0.3
	7.5	88	-0.3	-0.2/+0.1
	6.4	85	-0.4	-0.2/+0.1
	4.5	78	0.1	-0.2/+0.1